Predicting *in vivo* glioma growth with the reaction diffusion equation constrained by quantitative magnetic resonance imaging data

2015 Phys. Biol. 12 046006

(http://iopscience.iop.org/1478-3975/12/4/046006)

IOP Publishing Phys. Biol. 12 (2015) 046006 doi:10.1088/1478-3975/12/4/046006

Physical Biology

PAPER

RECEIVED
25 November 2014

REVISED
26 April 2015

ACCEPTED FOR PUBLICATION
6 May 2015

PUBLISHED
4 June 2015

Predicting *in vivo* glioma growth with the reaction diffusion equation constrained by quantitative magnetic resonance imaging data

David A Hormuth II[1,3], Jared A Weis[1,2], Stephanie L Barnes[1,2], Michael I Miga[1,2,3,6], Erin C Rericha[4], Vito Quaranta[5] and Thomas E Yankeelov[1,2,3,4,5]

[1] Vanderbilt University Institute of Imaging Science, Vanderbilt University, Nashville, TN, USA
[2] Departments of Radiology and Radiological Sciences, Vanderbilt University, Nashville, TN, USA
[3] Biomedical Engineering, Vanderbilt University, Nashville, TN, USA
[4] Physics and Astronomy, Vanderbilt University, Nashville, TN, USA
[5] Cancer Biology, Vanderbilt University, Nashville, TN, USA
[6] Neurological Surgery, Vanderbilt University, Nashville, TN, USA

E-mail: thomas.yankeelov@vanderbilt.edu

Keywords: mathematical model, cancer, forecast, glioma

Supplementary material for this article is available online

Abstract

Reaction–diffusion models have been widely used to model glioma growth. However, it has not been shown how accurately this model can predict future tumor status using model parameters (i.e., tumor cell diffusion and proliferation) estimated from quantitative *in vivo* imaging data. To this end, we used *in silico* studies to develop the methods needed to accurately estimate tumor specific reaction–diffusion model parameters, and then tested the accuracy with which these parameters can predict future growth. The analogous study was then performed in a murine model of glioma growth. The parameter estimation approach was tested using an *in silico* tumor 'grown' for ten days as dictated by the reaction–diffusion equation. Parameters were estimated from early time points and used to predict subsequent growth. Prediction accuracy was assessed at global (total volume and Dice value) and local (concordance correlation coefficient, CCC) levels. Guided by the *in silico* study, rats ($n = 9$) with C6 gliomas, imaged with diffusion weighted magnetic resonance imaging, were used to evaluate the model's accuracy for predicting *in vivo* tumor growth. The *in silico* study resulted in low global (tumor volume error <8.8%, Dice >0.92) and local (CCC values >0.80) level errors for predictions up to six days into the future. The *in vivo* study showed higher global (tumor volume error >11.7%, Dice <0.81) and higher local (CCC <0.33) level errors over the same time period. The *in silico* study shows that model parameters can be accurately estimated and used to accurately predict future tumor growth at both the global and local scale. However, the poor predictive accuracy in the experimental study suggests the reaction–diffusion equation is an incomplete description of *in vivo* C6 glioma biology and may require further modeling of intra-tumor interactions including segmentation of (for example) proliferative and necrotic regions.

1. Introduction

Mathematical models have been constructed to describe tumor growth and invasion over a large range of spatial scales (nm to cm) and temporal scales (ns to years). Substantial discussions have focused on translating these models to clinical care with the long term goal of providing clinicians with patient-specific predictions of future tumor growth and therapy response in order to optimally select and guide patient therapy [1–3]. Approaches for patient-specific predictions may focus on changes in a single property such as tumor volume, or changes in tumor growth as a function of several related properties (e.g., cellularity, vascularity, nutrient distribution). Models that focus on the change in a single tumor property can be parameterized readily with experimental data [4, 5], but may fail to capture spatial and temporal tumor heterogeneity of, for example, cellularity, vasculature density, proliferation rates, and the level of response

(or lack thereof) of cells to treatment that is observed within tumors [6, 7]. Patient-specific models that capture a tumor's spatial and temporal heterogeneity could be used to more accurately describe the delivery of treatment and subsequent response [8–11]. Unfortunately, modeling these characteristics frequently requires knowledge of parameters that can only be measured by highly invasive methods or within idealized (*in vitro*) settings [12–15]. The reliance of the existing modeling literature on parameters that are either extraordinarily difficult or impossible to measure non-invasively fundamentally limits their clinical application. Recasting these models in terms of parameters measured via non-invasive imaging measurements would dramatically improve the clinical relevance of patient-specific tumor growth predictions [1].

Magnetic resonance imaging (MRI) and positron emission tomography (PET) can be used to provide an array of non-invasive, quantitative, and functional measurements in 3D and at multiple time points of tumor growth. More specifically, MRI and PET can provide measurements of cellularity [16], blood volume [17, 18], blood flow [17, 18], hypoxia [19], oxygen saturation [20], and metabolism [21]. Additionally, the ability to make repeatable, non-invasive, spatially discretized, quantitative measurements of tumor growth supports the development, testing, and refinement of mathematical descriptions of *in vivo* tumor growth. Several groups [1, 5, 22–29] have incorporated imaging measurements from MRI, PET, and x-ray computed tomography into mathematical models of tumor growth. Preliminary efforts in both breast [23] and pancreatic [24] cancers, have shown that patient specific imaging data can potentially accurately predict future tumor growth. This, however, has not been demonstrated for gliomas.

One common model for glioma growth is the reaction–diffusion model, whereby the spatio-temporal change in tumor cellularity is due to proliferation and invasion (described by random diffusion) of tumor cells. The proliferation and invasion of cells are typically characterized with a proliferation rate and a diffusion coefficient, respectively. The reaction–diffusion model of glioma growth described by Swanson *et al* [29], uses proliferation and diffusion coefficients of tumor cells estimated from T_2-weighted and post-contrast T_1-weighted MRI data obtained at two time points. The estimated tumor cell proliferation and diffusion values can then be used to simulate tumor growth following surgical resection [29] or simulate a virtual control to assess patient response to radiotherapy [25]. Jbadbi *et al* [28] extended this approach by allowing anisotropic diffusion of tumor cells by replacing the diffusion coefficient with a diffusion tensor measured using diffusion tensor imaging. The authors showed that simulated anisotropic tumor growth better matched the shape of glioma growth observed in patients. Spatially varying estimates of diffusion and proliferation were included in the work of Ellingson *et al* [27]. In this work, serial diffusion weighted MR images were used to develop a voxel-wise analytical solution (when certain assumptions are satisfied) to a reaction–diffusion model of glioma growth. The proliferation and diffusion values were compared to MR spectroscopy measurements, but these values were not used to simulate tumor growth. Another extension of the reaction–diffusion model is the incorporation of mechanical properties of healthy and tumor tissue into a description of tumor growth [23, 24, 26, 30]. The work of Hogea *et al* [26] showed the benefit of incorporating mechanical deformations caused by the invading tumor growth into a reaction–diffusion model. Their effort also demonstrated the means to invert their model system to estimate parameters from imaging data.

In this work we use a reaction–diffusion model of glioma growth with proliferation and diffusion values estimated from quantitative *in vivo* imaging data to predict future tumor growth and then validate (or refute) that prediction by direct comparison to future *in vivo* measurements. Using an *in silico* tumor we first developed the means to accurately estimate model parameters and assessed the accuracy of tumor growth predictions. We then performed the analogous *in vivo* study, where model parameters were estimated from serial diffusion-weighted MRI data in a murine model of glioma to predict future tumor status which could then be directly compared to experimental outcome. The *in silico* experiments show that model parameters can be accurately estimated from tumor growth datasets and then used to predict future tumor growth with low global and local errors. However, when the approach is applied to *in vivo* glioma measurements, it is shown that the reaction–diffusion model provides poor predictive ability of future tumor growth.

2. Materials and methods

2.1. Modeling approach

The reaction–diffusion equation describes the spatio-temporal rate of change in tumor cell number and distribution due to the random movement of tumor cells (diffusion; the first term on the right-hand side of equation (1)), and proliferation (reaction; the second term on the right-hand side of equation (1)):

$$\frac{\partial N(\bar{x}, t)}{\partial t} = \nabla \cdot \left(D(\bar{x}) \nabla N(\bar{x}, t) \right) + k(\bar{x}) N(\bar{x}, t) \left(1 - \frac{N(\bar{x}, t)}{\theta} \right), \quad (1)$$

where $N(\bar{x}, t)$ is the number of tumor cells at three-dimensional position $\bar{x}$ and time t, $D(\bar{x})$ is the tumor cell diffusion coefficient at position $\bar{x}$, $k(\bar{x})$ is the net tumor cell proliferation at position $\bar{x}$, and θ is the tumor cell carrying capacity. Note that the proliferation term varies temporally as a function of cell

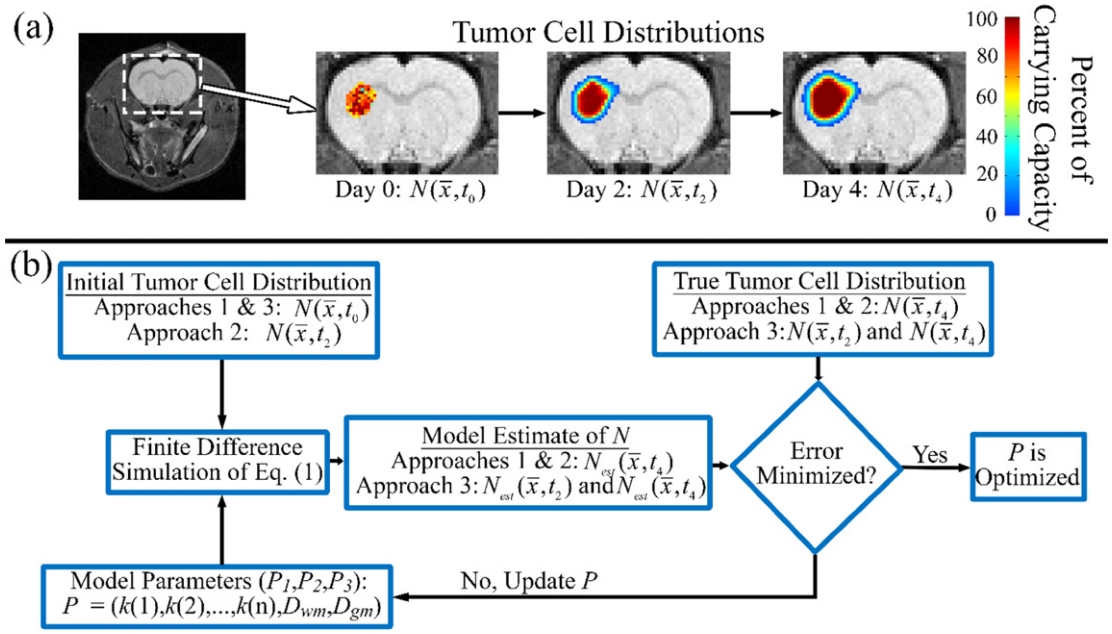

Figure 1. Parameter optimization approach. Panel (a) shows a central anatomical axial slice through the rat brain and cropped images of the *in silico* tumor cell distributions at days 0, 2, and 4. Panel (b) shows the model parameter optimization approach used for the *in silico* and *in vivo* studies. The process starts with an initial distribution of tumor cells and an initial guess for P. A finite difference simulation of equation (1) using the initial P and the initial tumor cell distribution is used to 'grow' a model estimate of N for four days. The error between N_{est} at day 4 (or days 2 and 4 for approach 3) and N is calculated. When the error between N_{est} and N is minimized, parameter optimization ceases and the model parameters are set to the current values of P. However, if the error is not minimized, P is updated and parameter optimization continues.

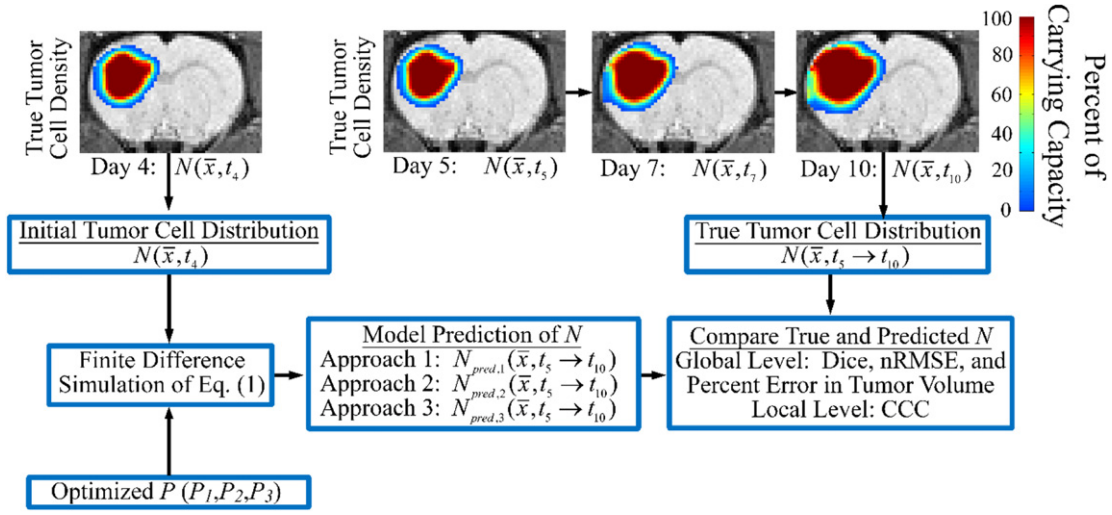

Figure 2. Predicted tumor growth modeling approach. This figure shows the modeling approach for predicting future tumor growth for the *in silico* and *in vivo* studies. The tumor growth prediction model is initialized with N from day 4 as well as the optimized parameters P. N at day 4 and P are used in a finite difference simulation of equation (1) to 'grow' the tumor for 6 days resulting in a model prediction of N (i.e., N_{pred}). This modeling approach is repeated for each set of model parameters (P_1, P_2, P_3). The error between N_{pred} and N at days 5 through 10 is calculated at the global level (Dice similarity coefficient, nrms error, and percent error in tumor volume) and at the local level (CCC).

density, $N(\bar{x}, t)$, although it is assumed that the proliferation rate, $k(\bar{x})$, is temporally constant. As described below, quantitative diffusion weighted magnetic resonance imaging (DW-MRI) provides estimates of $N(\bar{x}, t)$. These data are obtained at multiple time points, early in the tumor's life cycle, and used to solve an inverse problem using equation (1) to return estimates of $k(\bar{x})$ for each voxel within the tumor, and two $D(\bar{x})$ values: one for white matter (D_{wm}) and one for gray matter (D_{gm}). The forward evaluation of equation (1) is solved using a three dimension in space, fully explicit finite difference (FD) in time simulation

written in Matlab (Mathworks, Natick, MA). The simulation domain has no diffusive flux of tumor cells at brain tissue boundaries (i.e., at the skull) and the grid spacing matches the spatial resolution of the MRI data ($\Delta x = 250\ \mu$m, $\Delta y = 250\ \mu$m, $\Delta z = 1000\ \mu$m). The simulation time step was set at 0.01 days.

2.2. *In silico* experiments

Figures 1 and 2 show the approach for the *in silico* experiments. An initial distribution of tumor cells, $N(\bar{x}, t_0)$, was seeded within a rat brain domain. A spatial map of k was determined from DW-MRI estimates of $N(\bar{x}, t)$ from a C6 glioma bearing rat using equation (2):

$$k(\bar{x}) = -\log\left(N(\bar{x}, t_1)/N(\bar{x}, t_0)\right)/(t_1 - t_0), \quad (2)$$

where $N(\bar{x}, t_0)$ and $N(\bar{x}, t_1)$ represent the distribution of cells at time t_0 and t_1, respectively, while $k(\bar{x})$ remained constant in time. The initial model parameters, or P_{true} ($P = (k(1), k(2), \ldots k(n), D_{\text{gm}}, D_{\text{wm}})$, where n is the number of voxels within the tumor), were selected by iteratively scaling $k(\bar{x})$ until a 12 fold increase in total tumor volume was observed over 10 days, matching the average observed tumor volume increase observed in the *in vivo* study. An FD simulation of equation (1) with an initial distribution of tumor cells $N(\bar{x}, t_0)$ and parameters P_{true} was used to grow an *in silico* tumor for 10 days (1000 time steps/iterations). Tumor cell distributions, $N(\bar{x}, t)$, were then sampled at days 0, 2, and 4 thru 10. Panel (a) in figure 1 shows a central anatomical axial slice through a rat head and cropped images of the *in silico* tumor cell distribution seeded at day 0 and 'grown' to days 2 and 4. Three different combinations of these three time points were then used to estimate three sets of model parameters (P_1, P_2, and P_3). P_1 was estimated using tumor cell measurements from days 0 and 4 ($N(\bar{x}, t_0)$ and $N(\bar{x}, t_4)$, respectively). P_2 was estimated using tumor cell measurements from days 2 and 4 ($N(\bar{x}, t_2)$ and $N(\bar{x}, t_4)$, respectively), while P_3 was estimated using tumor cell measurements from days 0, 2, and 4 ($N(\bar{x}, t_0)$, $N(\bar{x}, t_2)$, and $N(\bar{x}, t_4)$, respectively). Panel (b) in figure 1 shows the parameter optimization approach for these model parameters (P_1, P_2, and P_3). For each set of estimated parameters (P_1, P_2, and P_3) a FD simulation of equation (1) was initialized with $N(\bar{x}, t_0)$ (for P_1 and P_3) or $N(\bar{x}, t_2)$ (for P_2) and used to grow a tumor to day 4 resulting in a model estimate of N for each parameter set ($N_{\text{est},1}$, $N_{\text{est},2}$, and $N_{\text{est},3}$). The error between N and $N_{\text{est},1}$, $N_{\text{est},2}$, and $N_{\text{est},3}$, respectively, was calculated. If this error is minimized, the optimal values of P_1, P_2, and P_3 have been determined, otherwise P_1, P_2, and P_3 are updated with new values. The optimized P values are then used to predict future tumor growth.

Figure 2 shows the modeling approach for predicting future tumor cell distributions. For each set of optimized parameters (P_1, P_2, and P_3) an FD simulation of equation (1) was used to 'grow' the tumor from day 4 to day 10 (6 days; 600 iterations) resulting in predicted tumor cell distributions for each parameter set ($N_{\text{pred},1}(\bar{x}, t_{5-10})$, $N_{\text{pred},2}(\bar{x}, t_{5-10})$, and $N_{\text{pred},3}(\bar{x}, t_{5-10})$, respectively). Error between the true N and N_{pred} was calculated at both the global and local levels by calculating the percent error in tumor volume, the Dice similarity coefficient, the normalized root mean square error (nrms error), and the concordance correlation coefficient (CCC).

2.3. *In vivo* experiments

All experimental procedures were approved by Vanderbilt University's Institutional Animal Care and Use Committee. Female Wistar rats ($n = 9$, 236–263 g) were anesthetized, given analgesics, and inoculated with C6 glioma cells (1×10^5) via stereotaxic injection. During each MRI procedure body temperature was maintained near 37 °C by a flow of warm air directed over the animal and respiration was monitored using a pneumatic pillow. Each rat was anesthetized using 2% isoflurane in 98% oxygen for all surgical and imaging procedures. Rats were imaged beginning 10 days post-surgery (defined as day 0). Rats were imaged up to 10 days after the first imaging time point. The first three imaging measurements for all rats occurred on days 0, 2, and 4. Rats 1–3 were then imaged on days 5, 8, and 10. Rats 4–5 were imaged on days 5, 6, and 9. Rat 6 was imaged on days 5, 6, 8 and 10, while rats 7–8 were imaged only on days 5 and 6. Rat 9 was only imaged at one additional time on day 5.

MRI was performed on a 9.4 T horizontal-bore magnet (Agilent, Santa Clara, CA, USA). The animal's head was positioned in a 38 mm diameter Litz quadrature coil (Doty Scientific, Columbia, SC, USA) and was secured by a bite bar. All MR images were sampled with a $128 \times 128 \times 16$ matrix acquired over a $32 \times 32 \times 16$ mm^3 field of view. In order to facilitate the modeling, the imaging volumes obtained at time points two through the end of the experiment were registered to the first time point via a mutual information based rigid registration algorithm performed at the scanner [31]; this ensures that the image volumes obtained at each time point are very nearly identical (see supplementary figures 1–3 for example registration results). A T_1 map was produced using data from an inversion-recovery snapshot experiment with TR/TE = 5000/3 ms, TI (inversion time) = (8 TIs logarithmically spaced between 200 and 4000 ms), and two averaged excitations.

DW-MRI was acquired using a pulsed fast spin echo diffusion sequence in three orthogonal diffusion encoding directions with b-values of 0, 300, 500, 700, 900, and 1100 s mm^{-2}, and $\Delta/\delta = 25$ ms/2 ms. The apparent diffusion coefficient (ADC) was estimated on a voxel basis using a two parameter fit of the DW-MRI data [32]. To determine $N(\bar{x}, t)$, the ADC values from the DW-MRI data are then transformed to estimate cell number [33, 34] using equation (3):

$$N\left(\bar{x},\, t\right) = \theta\left(\frac{\mathrm{ADC_w} - \mathrm{ADC}\left(\bar{x},\, t\right)}{\mathrm{ADC_w} - \mathrm{ADC_{min}}}\right), \qquad (3)$$

where θ represents the tumor cell carrying capacity, $\mathrm{ADC_w}$ is the ADC of free water at 37° C ($2.5 \times 10^{-3}\ \mathrm{mm^2\ s^{-1}}$) [32], $\mathrm{ADC}(\bar{x},\, t)$ is the ADC value at position $\bar{x}$ and time t, and $\mathrm{ADC_{min}}$ is the minimum ADC value which corresponds to the voxel with the largest number of cells. The carrying capacity, θ, was calculated for each imaging voxel assuming spherical tumor cells with a packing density of 0.7405 [35] with an average cell volume of 908 $\mu\mathrm{m}^3$ [36].

Tumor regions-of-interest (ROI) were manually placed at each time point using the T_1 maps. ADC measurements within these ROI's were then transformed to tumor cell number using equation (3). T_1 maps were used to define tumor, white, and gray matter regions in the MR images.

Similar to the *in silico* experiments, three sets of model parameters (P_1, P_2, and P_3) were then estimated for each rat. We note that the time and spatial origin of the tumor (as mentioned in Hogea *et al* [26]) was not determined as tumor growth simulations were initialized with tumor cellularity measurements from DW-MRI. The estimated parameters for each rat (parameters for rat 1; $P_{R1,1}$, $P_{R1,2}$, and $P_{R1,3}$) were used in a FD simulation of equation (1) to 'grow' simulated tumors from day 4 to day 10 (6 days; 600 iterations) resulting in predicted tumor cell distributions for each parameter set (predicted $N(\bar{x},\, t)$ for rat 1; $N_{R1,pred,1}(\bar{x},\, t_{5-10})$, $N_{R1,pred,2}(\bar{x},\, t_{5-10})$, and $N_{R1,pred,3}(\bar{x},\, t_{5-10})$, and, respectively).

The three different time point combinations from the *in vivo* data sets were also fit to a model substituting a spatially invariant proliferation rate (k_{ROI}) for the spatially variant proliferation rate ($k(\bar{x})$); i.e., $k(\bar{x}) \equiv k_{ROI}$ in equation (1).

2.4. Numerical methods

A Levenberg–Marquardt weighted least squares nonlinear optimization, implemented with a regularization parameter described in Joachimowicz *et al* [37, 38], was used to estimate model parameters (P_1, P_2, P_3) from tumor cell distribution measurements. All parameters were constrained to non-negative values. Prior to estimating P a 3×3 Gaussian filter was applied to each slice of $N(\bar{x},\, t)$ to reduce the effects of noise within individual voxels. During the optimization scheme, k was estimated voxel-wise in areas within the tumor ROI and assigned 0 elsewhere. Additionally, D_{wm} and D_{gm} values were assigned region-wise using a white and gray matter map. The optimized parameters were determined when the objective function, equation (4), was minimized:

$$\sum_{t=t_i}^{t_f}\left(\left(\sum_{\bar{x}=1}^{\bar{x}_i=n}\left(N\left(\bar{x},\, t\right)\right)\right)^{-1} \cdot \left(\sum_{\bar{x}=1}^{\bar{x}=n}\left(N_{est}\left(\bar{x},\, t\right) - N\left(\bar{x},\, t\right)\right)^2\right)\right), \qquad (4)$$

where t_i is the initial time point, t_f is the final time point, n is the total number of voxels within the tumor, and $N_{est}(\bar{x},\, t)$ is the model estimate of N using the current parameter set. For P_1 and P_2 optimizations, t_i and t_f were equal to day 4. For P_3 optimization t_i was equal to day 2 and t_f was equal to day 4.

To assess the effect of noise in ADC measurements on estimates of P, *in silico* parameter optimization was repeated ($N = 100$) for each set of parameters (P_1, P_2, P_3) with noise added to $N(\bar{x},\, t)$ from a normal distribution with a zero mean and a standard deviation of 3.3% of the carrying capacity (selected based on the reproducibility of ADC measurements *in vivo* [32]).

After optimization of P, these values were used in a FD implementation of equation (1), initialized with the tumor cell distribution at day 4 ($N(\bar{x},\, t_4)$), to 'grow' a predicted tumor from day 4 thru 10 (600 iterations). Throughout the FD simulation, as the tumor expanded into regions where an estimate of k was unavailable, k was assigned using a local average of available non-zero k's within a $3 \times 3 \times 3$ kernel.

The accuracy of P estimated from the *in silico* dataset was evaluated by computing the percent error between the true, P_{true}, and the estimated parameter sets (P_1, P_2, and P_3), the Pearson correlation coefficient (PCC), and the CCC (similar to the PCC but with a penalty for data that do not lie on the line of unity) [39]. A Bland–Altman analysis was also performed between the true, P_{true}, and the estimated (P_1, P_2, and P_3) parameter sets. For the *in vivo* study, agreement between P_1, P_2, and P_3 estimates of $k(\bar{x})$ was assessed by calculating the PCC and CCC for P_1 and P_2, P_1 and P_3, and P_2 and P_3. For both the *in vivo* and *in silico* studies error between the predicted and true tumor growth was assessed at the global (i.e., volume) and local (i.e., voxel) levels. For the *in vivo* analysis, the tumor ROIs and measured cellularity from DW-MRI are taken as true tumor growth. At the global level, error was assessed by calculating the percent error in tumor volume, the nrms error, and the Dice similarity coefficient (a measure of spatial overlap between two data sets ranging from 0 (no overlap) to 1 (complete overlap); [40]). The percent error in tumor volume and nrms error were computed by comparing the true tumor volume and the tumor volumes predicted from FD simulations using P_1, P_2, and P_3 at days 5 thru 10. The Dice similarity coefficient was computed by comparing the spatial overlap between the true tumor ROIs and the tumor ROIs predicted from FD simulations using P_1, P_2, and P_3 at days 5 thru 10. At the local level, error was assessed by computing the CCC between N and N_{pred} at days 5 thru 10. For the *in vivo*

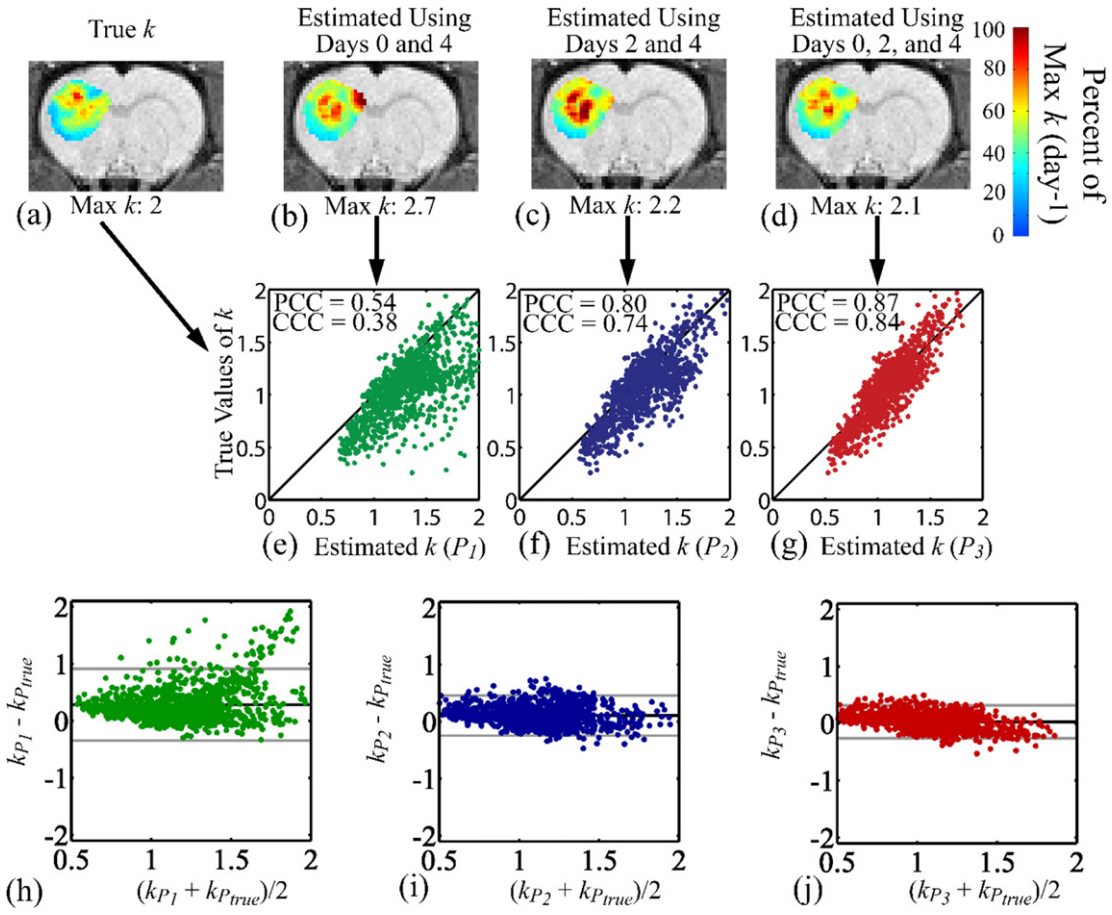

Figure 3. True and estimated proliferation rate maps from *in silico* study. The true (panel (a)) and estimated values (panels (b)–(d)) of k are shown for the *in silico* study. Panel (a) shows the true distribution of k used to 'grow' the *in silico* tumor. Panels (b)–(e) show example parameter maps of k estimated using days 0 and 4 (panel (b)), days 2 and 4 (panel (c)) and days 0, 2, and 4 (panel (d)). Panels (e)–(g) show the individual voxel values of the true k plotted against the estimated values of k from P_1, P_2, and P_3. Additionally panels (e)–(g) show the PCC and CCC values between the true k and the estimated k. k estimated from days 0 and 4 have more voxels that are overestimated resulting in a lower level of agreement (CCC = 0.38) compared to the other two approaches. The highest level of agreement and correlation (CCC = 0.84 and PCC = 0.87) between the estimated and true k was observed when days 0, 2, and 4 were used to estimate k. Panels (h)–(j) show the Bland–Altman analysis comparing the k_{P1}, k_{P2}, and k_{P3} to $k_{P\text{true}}$. The black lines represent the mean difference, while the gray lines represent the 95% confidence interval of those means. A lower mean difference was observed for k_{P3}–$k_{P\text{true}}$ (0.028) compared to k_{P1}– $k_{P\text{true}}$ (0.28) and k_{P2}–$k_{P\text{true}}$ (0.11).

study, paired t-tests were used to evaluate the differences between percent error in tumor volume, Dice, and CCC results observed with the spatially variant k and spatially invariant k models.

3. Results

3.1. *In silico* results

Illustrative results of the *in silico* experiments are shown figures 3–5 and summarized in table 1. Figure 3 shows the true distribution of k (panel (a)) used to 'grow' the *in silico* tumor, the estimated values of k (panels (b)–(d)), and plots of the true voxel values of k against the estimated values of k (panels (e)–(g)). Panels (b) and (e) show the results from parameters estimated from days 0 and 4. Both a low level of agreement (CCC = 0.38) and a weak linear relationship (PCC = 0.54) is observed between the true k and the k estimated using the P_1 data sets (k_{P1}). Additionally 88% of voxels in k_{P1} are overestimated. Parameters estimated using days 2 and 4 (panels (c) and (f)) showed an improved level of agreement (CCC = 0.74), stronger linear relationship (PCC = 0.80), and fewer overestimated voxels (72%) compared to k_{P1}. Using all three time points (panels (d) and (g)) resulted in the best level of agreement (CCC = 0.84), the strongest linear relationship (PCC = 0.87), and the fewest overestimated voxels (58%). Panels (h)–(j) show the Bland–Altman analysis for P_1, P_2, and P_3 compared to P_{true}. The black lines represent the mean difference while the gray lines represent the 95% confidence interval (CI). A larger 95% CI was observed for k_{P1}–$k_{P\text{true}}$ (−0.35 to 0.91) compared to k_{P2}–$k_{P\text{true}}$ (−0.25 to 0.46) and k_{P3}–$k_{P\text{true}}$ (−0.26 to 0.32).

Figure 4 shows the true (panel (a)) and the predicted tumor cell distributions (top rows in panels (b)–(d)) and the percent difference between the true and predicted distributions (bottom rows in panels (b)–(d)). Panel (b) shows the predicted N at day 5 using P_1, P_2, and P_3. The highest error between N and

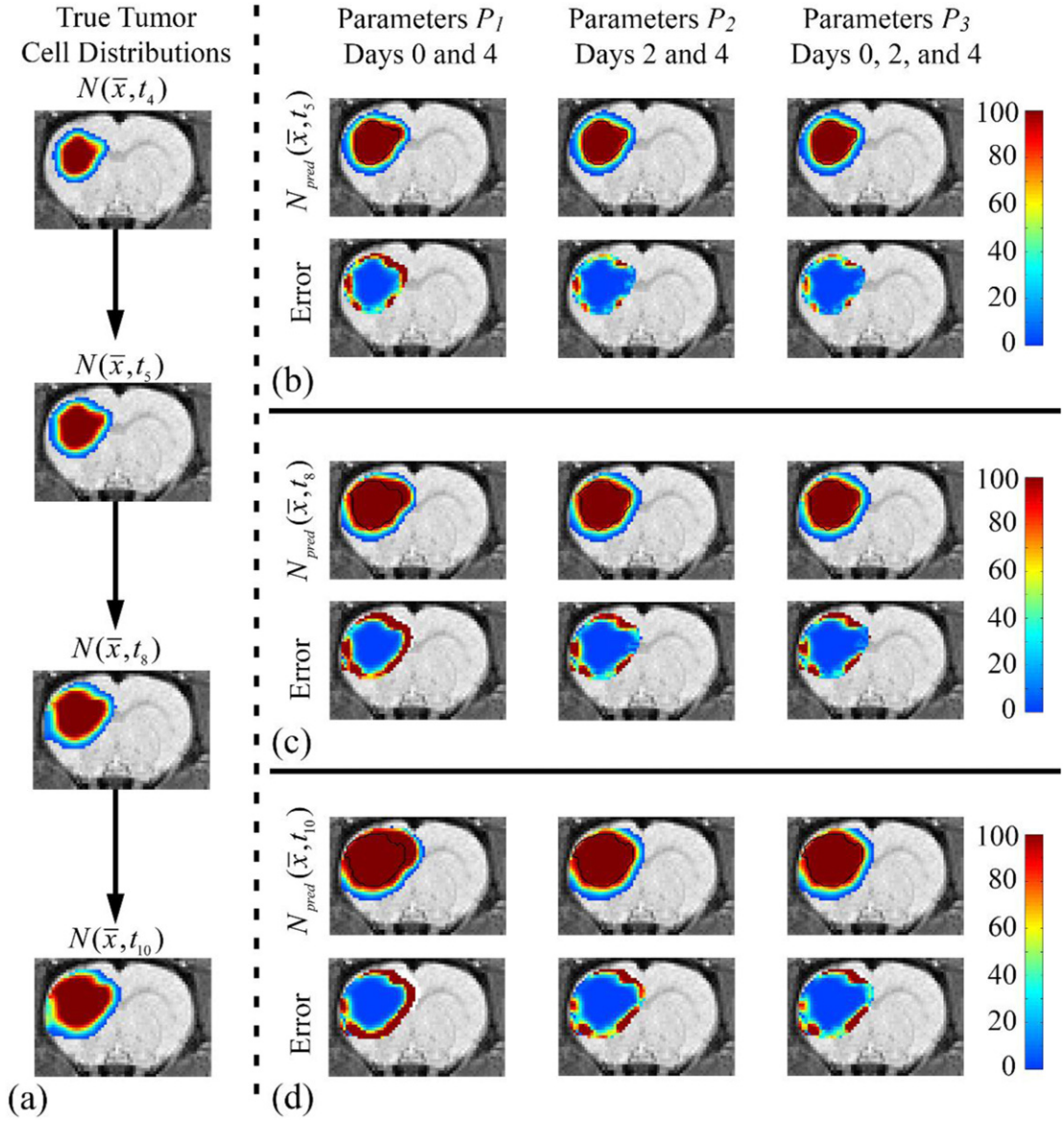

Figure 4. True and predicted tumor cell distributions for *in silico* study. The true and predicted tumor cell distributions for the *in silico* study are showed above. Panel (a) shows the true N at the central slice of the tumor volume on days 4, 5, 8, and 10. The predicted N (N_{pred}) and the error between N and N_{pred} for the same slice on days 5, 8, and 10 are shown in panels (b)–(d). The black outline displayed on N_{pred} in panels (b)–(d) represent the high cell density region from the true tumor cell distributions in panel (a). The color bars represent percent of the carrying capacity (top rows) and percent error (bottom rows). White regions observed in the percent error maps represent areas where no tumor cells were observed in the true data set. The top rows in panels (b)–(d) represent N_{pred}, while the bottom row represents the percent difference between N and N_{pred}. Additionally, the three columns in panels (b)–(d) represent the results using parameters P_1, P_2, and P_3. Increased error (greater than or equal to 100%) is observed at the periphery of the tumor relative to the interior of the tumor (less than 20%).

N_{pred} at day 5 was observed for parameters P_1 (mean ± standard error; $31.15 \pm 0.82\%$) compared to P_2 ($19.67 \pm 0.64\%$) and P_3 ($16.84 \pm 0.58\%$). As the tumor continues to grow, increased error is observed between N and N_{pred}. Generally, this error is increased at the periphery (greater than 100% error) relative to the interior (less than 40%). The predicted N at day 8 (panel (c)) resulted in increased mean error relative to day 5 for predictions using P_1 ($41.38 \pm 0.87\%$), P_2 ($28.03 \pm 0.68\%$) and P_3 ($26.03 \pm 0.64\%$). At the final time point (panel (d)), P_3 based predictions had a mean error ($29.51 \pm 0.65\%$) lower than P_1 ($45.93 \pm 0.90\%$) and P_2 ($30.83 \pm 0.67\%$) based predictions. The lowest cumulative error was observed for P_3 based predictions (nrms error; mean = 0.062, standard error = 1.33×10^{-2}) compared to P_1 based predictions (mean = 0.289, standard error = 2.51×10^{-2}) or P_2 based predictions (mean = 0.102, standard error = 1.19×10^{-2}).

The results of the ROI and voxel level analysis are shown in figure 5. Error in tumor volume generally increases the further out in time a prediction is made (panel (a)). Percent error in tumor volume ranged from 11.9 to 36.4% for P_1 based predictions, 3.1 to 13.6% for P_2 based predictions, and 0.8 to 8.8% for P_3 based predictions. All parameter sets, however,

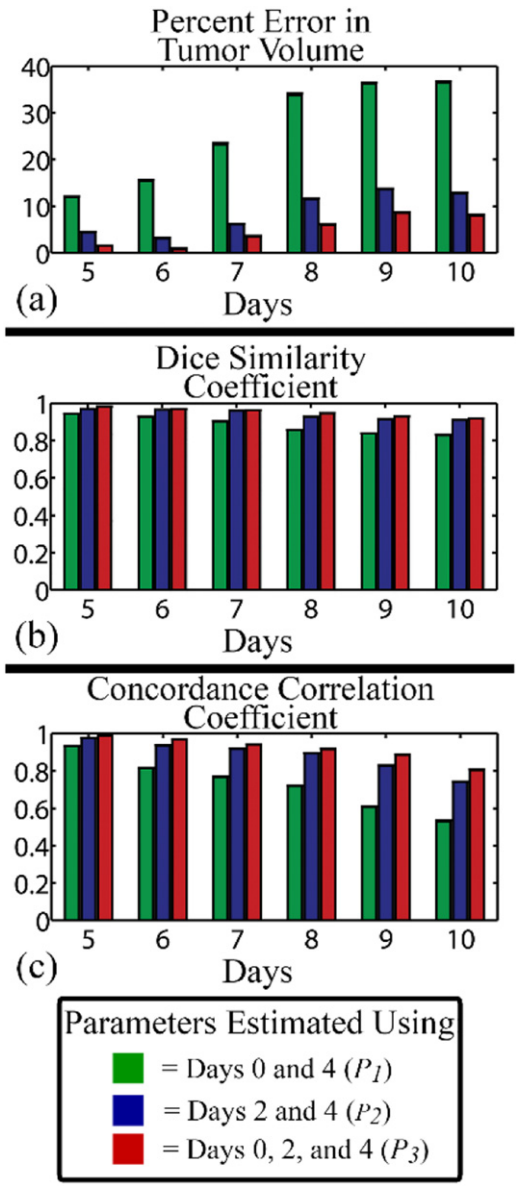

Figure 5. Global and local level error analysis for *in silico* study. Panels (a) and (b) show the result of global level error analysis while panel (c) shows the result of local level error analysis for the *in silico* experiments. The mean and standard error ($N = 100$) of each measurement is plotted at days 5 through 10. Panel (a) shows that less than 8.8% error is observed for all predictions when using parameters estimated from days 0, 2, and 4. Standard error in panel (a) is less than 0.32%. The Dice values (panel (b)) show all parameter sets result in a Dice value greater than 0.83. Panel (c), shows a steady decrease in the level of voxel agreement (decrease in CCC) over time for all sets of parameters. At each time point and for each error measurement there are significant differences between values from P_1 and P_2, P_1 and P_3, and P_2 and P_3 ($P \leqslant 0.05$). The standard error in panels (b) and (c) is less than 3.8×10^{-3}.

Table 1. Parameter estimation error from *in silico* experiments.

	Percent error: mean (standard error)		
	Days 0 and 4	Days 2 and 4	Days 0, 2, and 4
D_{wm}	−76.2 (0.3)	−49.5 (0.7)	−1.0 (0.5)
D_{gm}	−13.7 (0.3)	−6.2 (0.4)	−0.5 (0.2)
k	28.3 (3.9)	13.1 (2.1)	5.9 (1.8)

resulted in Dice values (panel (b)) greater than 0.83 at days 5 thru 10. An increased level of agreement was observed at the voxel level (panel (c)) for P_3 based predictions (CCC: 0.80–0.99) relative to P_1 based predictions (CCC: 0.53–0.93) and P_2 based predictions (CCC: 0.74–0.98).

Table 1 shows the mean percent error between the true values and estimated values of k, D_{wm}, and D_{gm}. Using all three time points resulted in less than 1.0% error in estimates of D_{wm}, whereas using two time points (days 0 and 4 or days 2 and 4) resulted in greater than 49.5% error. Less than 6.2% error was observed in estimates of D_{gm} when using days 2 and 4 or days 0, 2, and 4, while 13.7% error was observed when using days 0 and 4 to estimate model parameters. Similarly, the highest mean error in k was observed for parameters estimated from days 0 and 4 ($28.3 \pm 2.9\%$), while lower error was observed for the approaches using days 2 and 4 ($13.1 \pm 2.1\%$) and days 0, 2, and 4 ($5.9 \pm 1.8\%$).

3.2. *In vivo* results

The results of the *in vivo* experiments are shown in figures 6–8 and tables 2 and 3. Figure 6 shows the PCC (a) and CCC (b) analysis for all nine rats, as well as k_{P1}, k_{P2}, and k_{P3} from rats 3 (c)–(e) and 6 (f)–(h). The green bars in panels (a) and (b) represent the comparison of k_{P1} to k_{P2}, while the blue and red bars represent the k_{P1} to k_{P3} and k_{P2} to k_{P3} comparisons, respectively. A high level of correlation existed between k_{P1} and k_{P3} (mean PCC = 0.75, standard error = 0.05) and between k_{P1} and k_{P2} (mean PCC = 0.72, standard error = 0.09) compared to k_{P2} to k_{P3} (mean PCC = 0.46, standard error = 0.08). Similar comments apply to the CCC trends. Panels (c)–(h) show estimated k_{P1} (panels (c) and (f)), k_{P2} (panels (d) and (g)), and k_{P3} (panels (e) and (h)) for rats 3 and 6. Rat 3 (c)–(e) is an example of a rat with a high level of correlation (PCC: 0.68 to 0.88) but a low level of agreement (CCC: 0.08 to 0.34). Rat 6 (f)–(h), however, is an example of a rat with both a high level of correlation (PCC: 0.72 to 0.93), and a high level of agreement (CCC: 0.60 to 0.84).

Figure 7 shows the true (panel (a)) and the predicted tumor cell distributions (top rows in panels (b)–(d)) and the percent difference between the true and predicted distributions (bottom rows in panels (b)–(d)) for rat 1. The left column in panel (a) shows T_2-weighted images with a white box indicating the simulation domain and a black outline around the tumor. Panel (b) shows estimated k and the predicted N at day 5 using P_1, P_2, and P_3. Decreased k_{P1} (mean ± standard error; 0.08 ± 0.02 day^{-1}), k_{P2} (0.13 ± 0.03 day^{-1}), and k_{P3} (mean ± standard error; 0.08 ± 0.02 day^{-1}) were observed for the low cell density regions relative to the rest of the tumor (k_{P1}; 1.51 ± 0.06 day^{-1}, k_{P2}; 1.87 ± 0.10 day^{-1}, k_{P3}; 1.32 ± 0.05 day^{-1}). The highest error between N and N_{pred} at day 5 was

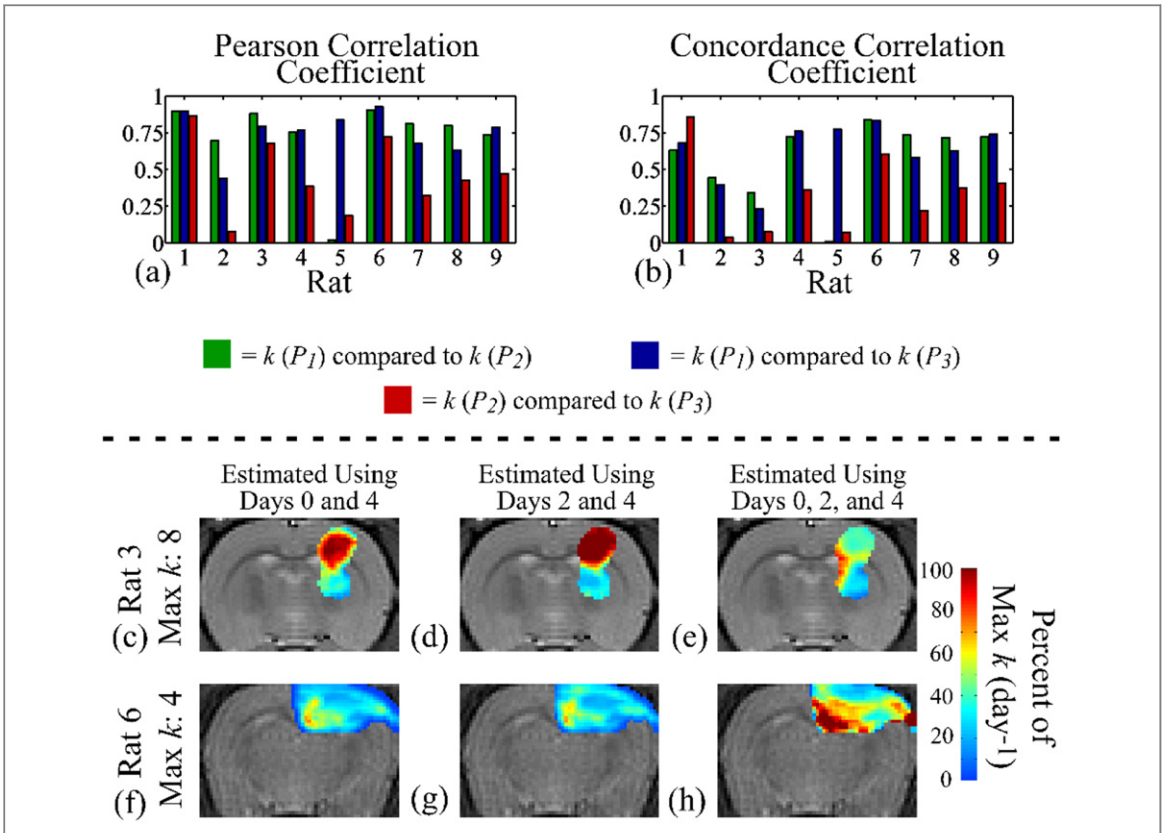

Figure 6. Estimated proliferation rate maps from *in vivo* study. Panels (a) and (b) show the results of the PCC and CCC analysis between k_{P1} to k_{P2} (green bars), k_{P1} to k_{P3} (blue bars), and k_{P2} to k_{P3} (red bars) for each rat. Higher agreement and correlation was observed between k_{P1} to k_{P2} and k_{P1} to k_{P3}, while weaker correlation and agreement was observed between k_{P2} to k_{P3}. Proliferation rate maps from the central slice of rat 3 (c)–(e) and 6 (f)–(h) are also shown above. Panels (c) and (f) show the estimated k_{P1}, while panels (d) and (g) show k_{P2} and panels (e) and (h) show k_{P3}. The proliferation rates in each image range from 0 to the maximum k of each rat (max $k = 8$ for rat 3, max $k = 4$ for rat 6). The proliferation maps demonstrate spatial heterogeneity of proliferation rates within the tumor. Additionally, the magnitude of k varies between the methods (i.e., using P_1, P_2, or P_3) used to estimate k.

observed for parameters P_3 (mean ± standard error; 17.80 ± 0.50%) compared to P_1 (17.07 ± 0.50%) and P_2 (17.12 ± 0.51%). Increased error (greater than or equal to 100% error) is observed between N and N_{pred} at both the periphery and in regions where N has low cell numbers (less than 50% of a voxels carrying capacity). This pattern is observed also in panels (c) and (d). Increased error at day 8 (panel (c)) was observed relative to day 5 (panel (b)) with P_1 predictions having the highest error (32.58 ± 0.63%) compared to P_2 (28.27 ± 0.57%) and P_3 (31.43 ± 0.61%). The predicted N at day 10 (panel (d)) shows an overestimation of tumor size for P_2 based predictions compared to P_1 or P_3 based predictions. However, at the voxel level the highest mean error was observed for P_1 based predictions (35.80 ± 0.54%) relative to P_2 (35.03 ± 0.53%) and P_3 (33.45 ± 0.51%) based predictions.

Figure 8 presents the global and local level error analysis for the *in vivo* experiments. Panels (a)–(c) show the results when a spatially variant k (i.e., $k(\bar{x})$) is estimated and panels (d)–(f) show the results for the spatially invariant estimated k (i.e., k_{ROI}). For the spatially variant k, percent error in tumor volume (panel (a)) for P_1, P_2, and P_3 based predictions ranged from 14 to 34%, 16 to 50%, and 12 to 29%, respectively. Lower Dice values (panel (b)) were observed compared to the *in silico* study and ranged from 0.67 to 0.81 for all approaches. Similarly, the *in vivo* study had decreased level of agreement (panel (c)) compared to the *in silico* study with CCC's less than 0.33 for all approaches. For the spatially invariant k, percent error in tumor volume (panel (d)) for P_1, P_2, and P_3 based predictions ranged from 36 to 58%, 36 to 77%, and 32 to 54%, respectively. The Dice values were also lower than the *in silico* study and ranged from 0.66 to 0.79. Lower agreement (CCC < 0.25) at the voxel level was also observed for the spatially invariant k approach compared to the spatially variant k approach. The spatially invariant k's percent error in tumor volume was significantly greater ($P < 0.05$) than the spatially variant k's results for all parameter sets. Similarly, both the Dice and CCC values were significantly smaller ($P < 0.05$) for the spatially invariant k predictions compared to the spatially variant k predictions.

The average diffusion estimates and the nrms error for both the spatially variant and invariant k models are shown in table 2. For the spatially variant k model fits, the mean D_{wm} ranged from 1.49×10^4 to 1.57×10^4 μm^2 day^{-1}, and the mean D_{gm} per animal ranged from 1.58×10^4 to 1.99×10^4 μm^2 day^{-1}. The cumulative error (nrms error) was lowest for P_3 based predictions (0.49) compared to P_1 (0.54) or P_2 (0.81)

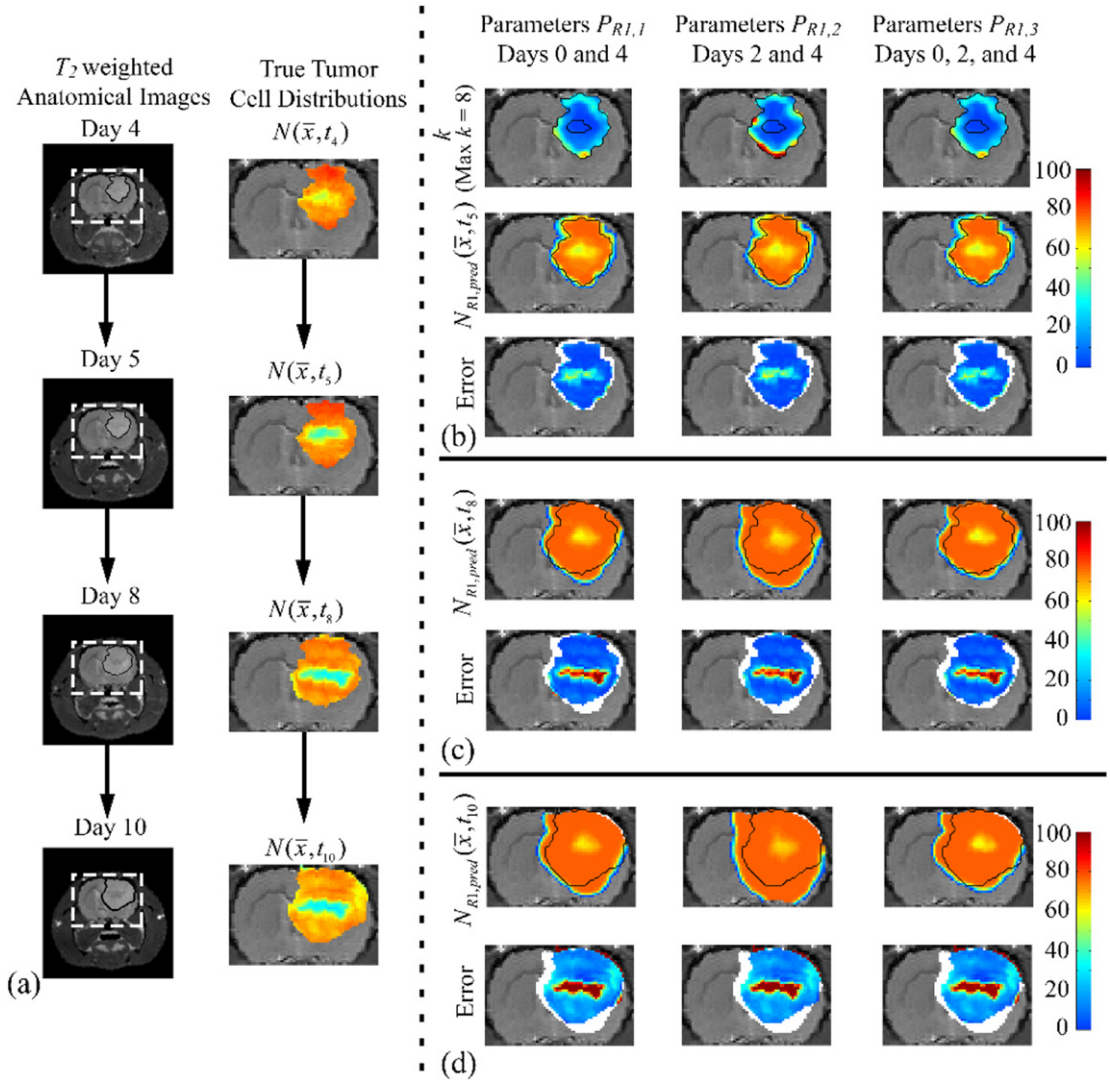

Figure 7. True and predicted tumor cell distributions for rat 1. The true and predicted tumor cell distributions for an example rat (rat 1) from the *in vivo* study are shown above. Panel (a) shows the T_2 weighted anatomical images (left column, black lines representing tumor ROI, white box representing simulation domain) and the true N (right column) at the central slice of the tumor volume on days 4, 5, 8, and 10. The predicted N (N_{pred}) and the error between N and $N_{\text{R1,pred}}$ for the same slice on days 5, 8, and 10 are shown in panels (b)–(d). The estimated k is also shown in panel (b). The color bars represent percent of max k value (top row in panel (b)), the percent of the carrying capacity (rows labeled '$N_{\text{R1,pred}}$'), and percent error (bottom rows). The black outline displayed within the k maps represent areas of low cell density on day 4. White regions observed in the percent error maps represent areas where no tumor cells were observed in the true data set. The black outline displayed on N_{pred} in panels (b)–(d) represent the tumor periphery observed in the true tumor cell distributions in panel (a). The top rows in panels (b)–(d) represent $N_{\text{R1,pred}}$, while the bottom row represents the percent difference between N and $N_{\text{R1,pred}}$. Additionally, the three columns in panels (b)–(d) represent the results using parameters $P_{R1,1}$, $P_{R1,2}$, and $P_{R1,3}$. Increased error (greater than or equal to 100%) is generally observed at the periphery of the tumor relative to the interior of the tumor (less than 20% error). Increased error between $N_{\text{R1,pred}}$ and N (greater than or equal to 100%) is also observed in areas where N has low cell numbers (less than 50% of a voxel's carrying capacity).

based predictions. The spatially invariant k model optimization resulted in higher diffusion values for both D_{wm} (greater than 3.05×10^4) and D_{gm} (greater than 3.50×10^4) compared to the spatially variant k results. Increased cumulative error (nrms error >1.04) was also observed compared to the spatially variant k results.

Table 3 shows the average proliferation rate for each rat from the spatially variant ($k(\bar{x})$, where $\overline{k(\bar{x})}$ is the average voxel-wise k estimated within the tumor) and the estimated spatially invariant proliferation rate (k_{ROI}). $\overline{k(\bar{x})}$ ranged from 0.51 to 4.06 day^{-1}, while k_{ROI} ranged from 0.94 to 9.94 day^{-1}. k_{ROI} was larger than $\overline{k(\bar{x})}$ for six rats for parameter estimates using day 0 and day 4, nine rats for days 2 and 4, and three rats when all three time points were used.

4. Discussion

The results of the *in silico* experiments indicate that the parameters within the reaction–diffusion equation (i.e., D_{wm}, D_{gm}, and k) can be accurately estimated and then used to accurately predict future tumor growth at the local and global levels, provided the tumor's growth is described by the reaction–diffusion

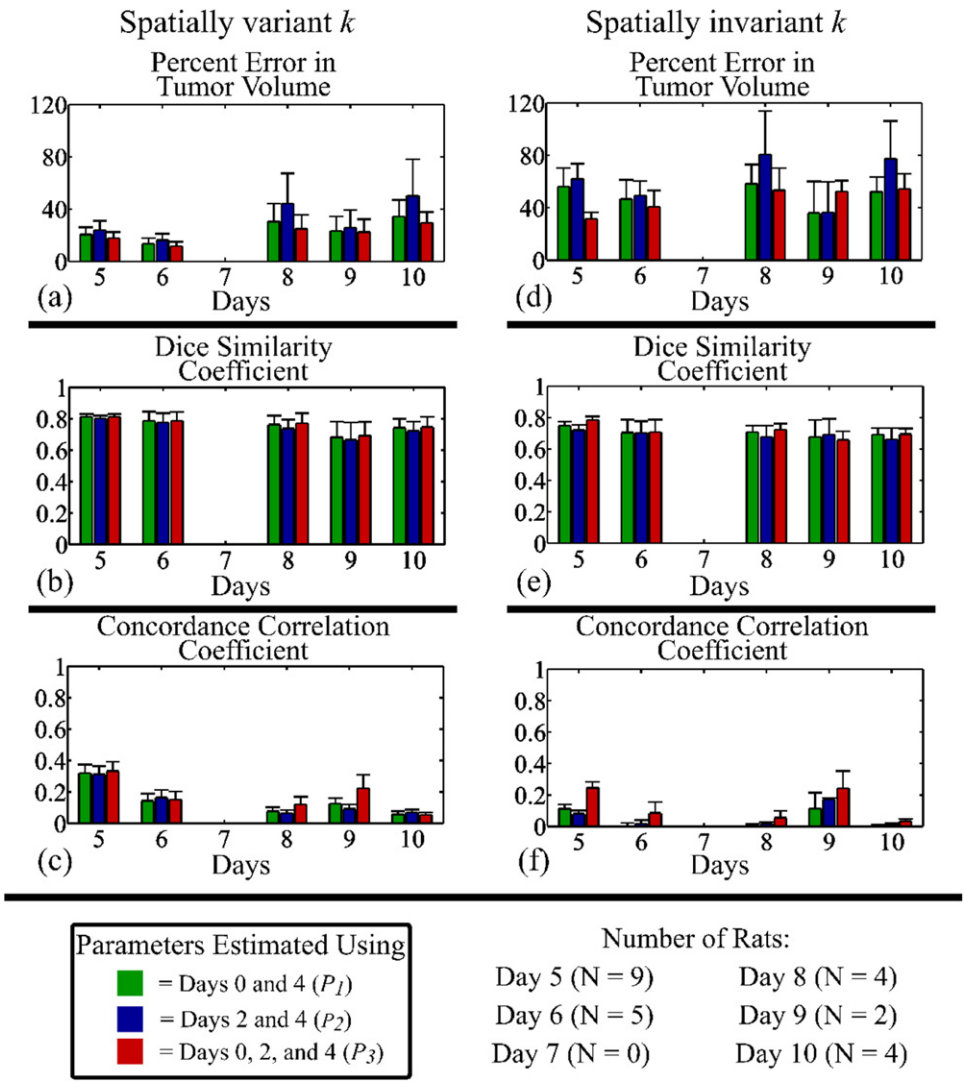

Figure 8. Global and local level error analysis for *in vivo* study. Panels (a)–(c) show the results for the spatially variant k predictions and panels (d)–(f) show the results for the spatially invariant k predictions. Panels (a) and (b) and (d) and(e) show the result of the global level error analysis, while panels (c) and (f) show the results of the local level error analysis for the *in vivo* experiments. The mean and standard error of each measurement is plotted at days 5 through 10. Panel (a) shows that greater than 11.7% error is observed for all predictions when using days 0, 2 and 4. No significant difference ($P > 0.05$) was observed between the results of the three different parameter sets. The Dice values (panel (b)) show that no significant difference ($P > 0.05$) was observed between the results using the three different parameter sets. Panel (c) shows a steady decrease in the level of voxel agreement (decrease in CCC) over time for all sets of parameters, but no significant difference ($P > 0.05$) between parameter estimation approaches. Predictions made with the spatially invariant k (panels (d)–(f)) resulted in increased percent error in tumor volume and decreased tumor volume agreement (lower Dice values) and decreased voxel level agreement (CCC < 0.25).

Table 2. Average diffusion parameter values and nrms error from *in vivo* experiments.

		Mean (standard error)		
		Days 0 and 4	Days 2 and 4	Days 0, 2, and 4
Spatially variant	D_{wm} (μm^2 day^{-1})	1.53×10^4 (3.71×10^3)	1.49×10^4 (4.71×10^3)	1.57×10^4 (4.15×10^3)
	D_{gm} (μm^2 day^{-1})	1.71×10^4 (2.87×10^3)	1.99×10^4 (3.86×10^3)	1.58×10^4 (4.81×10^3)
	nrms error	0.54 (0.15)	0.81 (0.29)	0.49 (0.13)
Spatially Invariant	D_{wm} (μm^2 day^{-1})	3.26×10^4 (1.09×10^4)	3.05×10^4 (1.01×10^4)	5.2×10^4 (2.07×10^4)
	D_{gm} (μm^2 day^{-1})	3.50×10^4 (1.13×10^4)	3.59×10^4 (8.60×10^3)	8.01×10^4 (1.99×10^4)
	nrms error	1.27 (0.35)	1.73 (0.55)	1.04 (0.28)

equation. While parameters estimated from data with experimentally observed noise does increase the error between the true and estimated values, when three time points are used the error between the true and observed parameters is less than 5.86%. Thus, the addition of a third time point decreases the sensitivity of the parameter optimization algorithm to approximately the same level of noise that is present in the

Table 3. Average k values from *in vivo* experiments.

		Mean (standard error), units: (day^{-1})		
		Days 0 and 4	Days 2 and 4	Days 0, 2, and 4
Rat 1	$\overline{k(\bar{x})}$	2.39 (0.03)	3.38 (0.05)	3.24 (0.04)
	k_{ROI}	2.38	4.22	1.54
Rat 2	$\overline{k(\bar{x})}$	1.51 (0.01)	0.84 (0.01)	1.78 (0.02)
	k_{ROI}	1.30	0.94	1.41
Rat 3	$\overline{k(\bar{x})}$	2.32 (0.04)	4.06 (0.07)	1.08 (0.02)
	k_{ROI}	2.11	8.32	1.53
Rat 4	$\overline{k(\bar{x})}$	1.62 (0.03)	1.54 (0.04)	1.50 (0.03)
	k_{ROI}	2.90	3.38	1.69
Rat 5	$\overline{k(\bar{x})}$	2.97 (0.08)	1.57 (0.03)	3.15 (0.11)
	k_{ROI}	5.75	2.44	2.13
Rat 6	$\overline{k(\bar{x})}$	0.64 (0.04)	0.51 (0.06)	0.94 (0.04)
	k_{ROI}	1.01	1.26	1.26
Rat 7	$\overline{k(\bar{x})}$	1.99 (0.03)	1.40 (0.03)	2.69 (0.03)
	k_{ROI}	2.76	5.31	1.94
Rat 8	$\overline{k(\bar{x})}$	2.59 (0.04)	1.88 (0.04)	2.63 (0.04)
	k_{ROI}	2.69	2.70	2.25
Rat 9	$\overline{k(\bar{x})}$	3.44 (0.07)	3.84 (0.07)	2.76 (0.06)
	k_{ROI}	9.94	8.19	2.07

$\overline{k(\bar{x})}$ is the average k estimated voxel-wise within the tumor
k_{ROI} is the spatially invariant k estimated for the tumor

measurement. The increased error observed for D_{wm} relative to D_{gm} may be explained due to only 4% of the voxels in the domain being identified as white matter. The limited number of voxels containing white matter most likely makes the model less sensitive to changes in D_{wm} compared to D_{gm}.

The results of the *in silico* study show the strength of both the estimated parameters and the forward evaluation algorithm as exhibited in the high level of overlap of tumor volumes (Dice values greater than 0.83 for P_1, P_2, and P_3) and strong agreement at the local level (CCC values greater than 0.80 for P_3; greater than 0.53 for P_1 and P_2) between N and N_{pred} (figure 5). The largest disagreements occur at the tumor edges. The simple propagation (local average) of proliferation rates outside of the parameter estimation region propagates errors and may need to be improved to incorporate additional information (e.g., local cellularity, distance from vasculature, and nutrient concentration; importantly such data is also available from clinically relevant, non-invasive imaging studies [41]). The significant differences in prediction errors (globally and locally) between the two time point approaches (P_1 and P_2) suggest the parameter optimization approach is sensitive to the spacing between measurements (P_1: 4 days, P_2: 2 days). Additionally, the lower error in P_2 based predictions compared to P_1 based predictions suggest that the tumor growth between days 2 and 4 is more representative of future growth than growth between days 0 and 4.

The *in vivo* experiments demonstrated greater error at both the global and local level compared to the *in silico* experiments. The increased error suggests that the reaction–diffusion equation is an incomplete description of C6 biology. The overestimation of tumor volume estimates suggests that overall tumor growth properties are changing between the estimation time points and the prediction time points. At the global level, the expansion of the tumor may be less restricted at earlier time points compared to later time points. At the local level, these changes may be the result of an increase or decrease in proliferation due to changes in the viability of the cells within a particular voxel. The very poor CCCs (less than 0.33, figure 8) similarly suggest that the reaction–diffusion equation provides a poor description of local properties. The reaction–diffusion equation does, however, provide tumor growth predictions that co-localize (Dice values greater than 0.62) with the true tumor volumes. Different from the *in silico* study, P_1 predictions had lower percent error in tumor volume (less than 34.4%) compared to P_2 based predictions (less than 50.1%). This suggests that the tumor growth over days 0 and 4 are more representative of future *in vivo* growth than the tumor growth over days 2 and 4. The larger distance between measurements allows potentially inconsistent growth rates between days 0 and 2 and days 2 and 4 to be averaged over 4 days, lessening the effects of non-representative volumetric growth on model estimates and predictions. Replacing the voxel-specific proliferation, $k(\bar{x})$, with a tumor-specific proliferation rate, k_{ROI}, resulted in larger global (increased percent error in tumor volume, decreased Dice values) and local (decreased CCCs) level errors. The decreased agreement between predicted and observed tumor ROIs (decreased Dice values) using k_{ROI} suggest that a spatially variant k is an important factor in predicting tumor geometry by allowing variations in regional tumor expansion. This factor may also contribute to the increased tumor volume error due to a more uniform expansion of tumor growth.

There are several limitations in this current approach. One limitation is the assumption that all tumor cells within a given voxel (spatially variant k) or within the tumor (spatially invariant k) follow the same proliferation rules. Within tumors there may be groups of actively proliferating cells as well as cells that are quiescent or necrotic [42]. In particular, necrotic tissues (which can be relatively large compared to total tumor volume) can strongly influence tumor growth [42] and patient prognosis [43, 44]. Models incorporating different proliferation rules have the potential to more accurately describe *in vivo* proliferation [45, 46]; however, it is challenging to initialize these models using non-invasive measurements. Although the proliferation model in this approach is limited, the spatially variant k lessens the potential error (relative to k_{ROI}) in this assumption by discretizing the tumor into individual regions that can have a proliferation rate that more closely captures local behavior. A second limitation is that proliferation rates, k, estimated from early time points are assumed to be constant for the remainder of the tumor growth. The logistic growth term in equation (1) allows for temporally variation of

the instantaneous growth rate as cell density increases or decreases, but it does not allow for the individual voxel proliferation rates to vary temporally over the course of the experiment; this is a fundamental limitation of this model as formulated. As *in vivo* tumors expand, the characteristics of a cell's environment will change and either accelerate or slow future cell proliferation. A more realistic model would incorporate these phenomena [12, 13] and adjust the spatio-temporal distribution of k throughout the simulation. These approaches, however, require model parameters that are extraordinarily difficult to measure non-invasively thereby limiting their application to subject-specific model predictions. This approach also does not consider the impact that tumor necrosis and edema may have on tumor cell proliferation [42, 47, 48] and the estimation of cellularity from ADC measurements (e.g., increased water diffusion may be observed in necrosis or necrosis adjacent regions due to breakdown of barriers to free water movement). However, there currently is not a widely accepted or validated method for segmenting necrosis and edema *a priori* in brain tumors. A third limitation is that as the tumor expands into voxels not included in the parameter estimation procedure (i.e., voxels outside of the tumor ROI determined at day 4), the proliferation rate in that voxel is then assigned as the average of the nearby known proliferation rates. This average value of the local k does not account for differences in environmental conditions, cell distributions, or cell phenotypes that may alter a voxel's k. A fourth limitation of equation (1) is that D is temporally fixed which results in tumor growth that is unrestricted (i.e., the model assumes that the tumor is growing into an empty space and does not incorporate the effects of the surrounding tissue [49]) and unresponsive to changes in microenvironment properties (e.g., extracellular matrix components, growth factors, tumor necrosis factor, matrix-metalloproteinase [50, 51]). This limitation can be amended through including more realistic terms such as mass effect [26, 52] to temporally adjust tumor migration behavior which may increase the predictive accuracy of the model. We do note, though, that the models which include the spatial-temporal evolution of D and k must carefully consider how the model parameters will be initialized (i.e., how are the values for the additional model parameters assigned) to provide subject-specific tumor growth predictions. The poor predictive strength of the current model and the temporally constant proliferation rates hinders the reliability of both untreated (and, most likely, treated) tumor growth predictions. Expanding the model to include an additional term to describe the effect of treatment (i.e., death rate as a function of drug dose or radiation dose) or fitting for a post-treatment proliferation rate would provide a platform to compare observed treatment response to predicted treatment response.

In conclusion, parameters can be accurately estimated and used to predict future tumor growth with low error at the global and local levels, provided that the tumor's growth is described by the reaction–diffusion equation. However, the *in vivo* experiments suggest that the reaction–diffusion model consisting of just tumor cell diffusion and logistic growth described by equation (1) provides an incomplete description of tumor growth and must be amended to provide better descriptions of *in vivo* C6 glioma growth in rats.

Acknowledgments

The authors thank Zou Yue for performing the animal surgeries. We thank the National Institutes of Health for funding through NCI R01CA138599, NCI R21CA169387, NCI U01CA174706, NCI R25CA092043, and the Vanderbilt-Ingram Cancer Center Support Grant (NIH P30CA68485). We thank the Kleberg Foundation for the generous support of our institute's imaging program. ECR holds a Career Award from the BWF. This work was partially supported by a pilot project from the Physical Sciences in Oncology Center at the H Lee Moffitt Cancer Center and Research Institute (PIs: Robert Gatenby, M D, Robert Gillies, PhD).

References

[1] Yankeelov T E, Atuegwu N, Hormuth D A, Weis J A, Barnes S L, Miga M I, Rericha E C and Quaranta V 2013 Clinically relevant modeling of tumor growth and treatment response *Sci. Transl. Med.* **5** 187ps9
[2] Gammon K 2012 Mathematical modelling: forecasting cancer *Nature* **491** S66–7
[3] Savage N 2012 Modelling: computing cancer *Nature* **491** S62–3
[4] Kim B, Chenevert T L and Ross B D 1995 Growth kinetics and treatment response of the intracerebral rat 9L brain tumor model: a quantitative *in vivo* study using magnetic resonance imaging *Clin. Cancer Res.* **1** 643–50
[5] Atuegwu N C, Arlinghaus L R, Li X, Welch E B, Chakravarthy B A, Gore J C and Yankeelov T E 2011 Integration of diffusion-weighted MRI data and a simple mathematical model to predict breast tumor cellularity during neoadjuvant chemotherapy *Magn. Reson. Med.* **66** 1689–96
[6] Paulus W and Peiffer J 1989 Intratumoral histologic heterogeneity of gliomas—a quantitative study *Cancer* **64** 442–7
[7] Wagner M, Nafe R, Jurcoane A, Pilatus U, Franz K, Rieger J, Steinbach J P and Hattingen E 2011 Heterogeneity in malignant gliomas: a magnetic resonance analysis of spatial distribution of metabolite changes and regional blood volume *J. Neurooncol.* **103** 663–72
[8] Russell S M, Elliott R, Forshaw D, Golfinos J G, Nelson P K and Kelly P J 2009 Glioma vascularity correlates with reduced patient survival and increased malignancy *Surg. Neurology* **72** 242–6
[9] Brown J M and Wilson W R 2004 Exploiting tumour hypoxia in cancer treatment *Nat. Rev. Cancer* **4** 437–47
[10] Suit H, Skates S, Taghian A, Okunieff P and Efird J T 1992 Clinical implications of heterogeneity of tumor response to radiation therapy *Radiother. Oncol.* **25** 251–60
[11] Au J L, Jang S H, Zheng J, Chen C-T, Song S, Hu L and Wientjes M G 2001 Determinants of drug delivery and transport to solid tumors *J. Control Release* **74** 31–46

[12] Gerlee P and Anderson A R A 2007 An evolutionary hybrid cellular automaton model of solid tumour growth *J. Theor. Biol.* **246** 583–603
[13] Cai Y, Xu S, Wu J and Long Q 2011 Coupled modelling of tumour angiogenesis, tumour growth and blood perfusion *J. Theor. Biol.* **279** 90–101
[14] Anderson A R A and Chaplain M A J 1998 Continuous and discrete mathematical models of tumor-induced angiogenesis *Bull. Math. Biol.* **60** 857–99
[15] McDougall S R, Anderson A R A and Chaplain M A J 2006 Mathematical modelling of dynamic adaptive tumour-induced angiogenesis: clinical implications and therapeutic targeting strategies *J. Theor. Biol.* **241** 564–89
[16] Koh D M and Collins D J 2007 Diffusion-weighted MRI in the body: applications and challenges in oncology *Am. J. Roentgenol.* **188** 1622–35
[17] Yankeelov T E and Gore J C 2009 Dynamic contrast enhanced magnetic resonance imaging in oncology: theory, data acquisition, analysis, and examples *Curr. Med. Imaging Rev.* **3** 91–107
[18] Østergaard L 2005 Principles of cerebral perfusion imaging by bolus tracking *J. Magn. Reson. Imaging* **22** 710–7
[19] Padhani A, Krohn K, Lewis J and Alber M 2007 Imaging oxygenation of human tumours *Eur. Radiology* **17** 861–72
[20] Christen T, Lemasson B, Pannetier N, Farion R, Segebarth C, Rémy C and Barbier E L 2011 Evaluation of a quantitative blood oxygenation level-dependent (qBOLD) approach to map local blood oxygen saturation *NMR Biomed.* **24** 393–403
[21] Kubota K 2001 From tumor biology to clinical PET: a review of positron emission tomography (PET) in oncology *Ann. Nucl. Med.* **15** 471–86
[22] Atuegwu N C, Gore J C and Yankeelov T E 2010 The integration of quantitative multi-modality imaging data into mathematical models of tumors *Phys. Med. Biol.* **55** 2429–49
[23] Weis J A, Miga M I, Arlinghaus L R, Li X, Chakravarthy A B, Abramson V, Farley J and Yankeelov T E 2013 A mechanically coupled reaction–diffusion model for predicting the response of breast tumors to neoadjuvant chemotherapy *Phys. Med. Biol.* **58** 5851–66
[24] Liu Y, Sadowski S M, Weisbrod A B, Kebebew E, Summers R M and Yao J 2014 Patient specific tumor growth prediction using multimodal images *Med. Image Anal.* **18** 555–66
[25] Neal M L *et al* 2013 Discriminating survival outcomes in patients with glioblastoma using a simulation-based, patient-specific response metric *PLoS One* **8** e51951
[26] Hogea C, Davatzikos C and Biros G 2008 An image-driven parameter estimation problem for a reaction–diffusion glioma growth model with mass effects *J. Math. Biol.* **56** 793–825
[27] Ellingson B, LaViolette P, Rand S D, Malkin M G, Connelly J M, Mueller W M, Prost R W and Schmainda K M 2011 Spatially quantifying microscopic tumor invasion and proliferation using a voxelwise solution to a glioma growth model and serial diffusion MRI *Magn. Reson. Med.* **65** 1131–43
[28] Jbabdi S, Mandonnet E, Duffau H, Capelle L, Swanson K R, Pélégrini-Issac M, Guillevin R and Benali H 2005 Simulation of anisotropic growth of low-grade gliomas using diffusion tensor imaging *Magn. Reson. Med.* **54** 616–24
[29] Swanson K R, Rostomily R C and Alvord E C 2008 A mathematical modelling tool for predicting survival of individual patients following resection of glioblastoma: a proof of principle *Br. J. Cancer* **98** 113–9
[30] Garg I and Miga M I 2008 Preliminary investigation of the inhibitory effects of mechanical stress in tumor growth *Proc. SPIE* **6918** 69182L
[31] Colvin D C, Loveless M E, Does M D, Yue Z, Yankeelov T E and Gore J C 2011 Earlier detection of tumor treatment response using magnetic resonance diffusion imaging with oscillating gradients *Magn. Reson. Imaging* **29** 315–23
[32] Whisenant J G, Ayers G D, Loveless M E, Barnes S L, Colvin D C and Yankeelov T E 2014 Assessing reproducibility of diffusion-weighted magnetic resonance imaging studies in a murine model of HER2+ breast cancer *Magn. Reson. Imaging* **32** 245–9
[33] Anderson A W, Xie J, Pizzonia J, Bronen R A, Spencer D D and Gore J C 2000 Effects of cell volume fraction changes on apparent diffusion in human cells *Magn. Reson. Imaging* **18** 689–95
[34] Atuegwu N C, Colvin D C, Loveless M E, Xu L, Gore J C and Yankeelov T E 2012 Incorporation of diffusion-weighted magnetic resonance imaging data into a simple mathematical model of tumor growth *Phys. Med. Biol.* **57** 225–40
[35] Martin I, Dozin B, Quarto R, Cancedda R and Beltrame F 1997 Computer-based technique for cell aggregation analysis and cell aggregation in *in vitro* chondrogenesis *Cytometry* **28** 141–6
[36] Rouzaire-Dubois B, Milandri J B, Bostel S and Dubois J M 2000 Control of cell proliferation by cell volume alterations in rat C6 glioma cells *Pflugers Arch.* **440** 881–8
[37] Joachimowicz N, Pichot C and Hugonin J-P 1991 Inverse scattering: an iterative numerical method for electromagnetic imaging *IEEE Trans. Antennas Propag.* **39** 1742–53
[38] Ou J, Ong R E, Yankeelov T E and Miga M I 2008 Evaluation of 3D modality-independent elastography for breast imaging: a simulation study *Phys. Med. Biol.* **53** 147
[39] Lin L I 1989 A concordance correlation coefficient to evaluate reproducibility *Biometrics* **45** 255–68
[40] Dice L R 1945 Measures of the amount of ecologic association between species *Ecology* **26** 297–302
[41] Yankeelov T E, Abramson R G and Quarles C C 2014 Quantitative multimodality imaging in cancer research and therapy *Nat. Rev. Clin. Oncol.* **11** 670–80
[42] Freyer J P 1988 Role of necrosis in regulating the growth saturation of multicellular spheroids *Cancer Res.* **48** 2432–9
[43] Lacroix M *et al* 2001 A multivariate analysis of 416 patients with glioblastoma multiforme: prognosis, extent of resection, and survival *J. Neurosurg.* **95** 190–8
[44] Iliadis G, Kotoula V, Chatzisotiriou A, Televantou D, Eleftheraki A, Lambaki S, Misailidou D, Selviaridis P and Fountzilas G 2012 Volumetric and MGMT parameters in glioblastoma patients: survival analysis *BMC Cancer* **12** 3
[45] Gevertz J L, Gillies G T and Torquato S 2008 Simulating tumor growth in confined heterogeneous environments *Phys. Biol.* **5** 036010
[46] Gyllenberg M and Webb G 1989 Quiescence as an explanation of Gompertzian tumor growth *Growth Dev. Aging* **53** 25–33
[47] Sherar M D, Noss M B and Foster F S 1987 Ultrasound backscatter microscopy images the internal structure of living tumour spheroids *Nature* **330** 493–5
[48] Folkman J and Hochberg M 1973 Self-regulation of growth in three dimensions *J. Exp. Med.* **138** 745–53
[49] Helmlinger G, Netti P A, Lichtenbeld H C, Melder R J and Jain R K 1997 Solid stress inhibits the growth of multicellular tumor spheroids *Nat. Biotech.* **15** 778–83
[50] Giese A, Bjerkvig R, Berens M E and Westphal M 2003 Cost of migration: invasion of malignant gliomas and implications for treatment *J. Clin. Oncol.* **21** 1624–36
[51] Demuth T and Berens M 2004 Molecular mechanisms of glioma cell migration and invasion *J. Neurooncol.* **70** 217–28
[52] Wong K L, Summers R, Kebebew E and Yao J 2014 Tumor growth prediction with hyperelastic biomechanical model, physiological data fusion, and nonlinear optimization *Medical Image Computing and Computer-Assisted Intervention—MICCAI 2014 SE–4* ed P Golland, N Hata, C Barillot, J Hornegger and R Howe (Cham: Springer) pp 25–32